

## Soft X-ray Emission Spectroscopy at ESRF Beamline 26 Based on a Helical Undulator

C. Dallera,<sup>a</sup> E. Puppini,<sup>a</sup> G. Trezzi,<sup>a</sup> N. Incorvaia,<sup>a</sup> A. Fasana,<sup>a</sup> L. Braicovich,<sup>a</sup> N. B. Brookes<sup>b</sup> and J. B. Goedkoop<sup>b</sup>

<sup>a</sup>Istituto Nazionale di Fisica della Materia, Department of Physics, Politecnico di Milano, Piazza Leonardo da Vinci 32, I-20133 Milano, Italy, and <sup>b</sup>European Synchrotron Radiation Facility, BP 220, F-38043 Grenoble, France

(Received 8 January 1996; accepted 8 May 1996)

A new soft X-ray spectrograph for X-ray emission spectroscopy excited by synchrotron radiation is presented. The apparatus is now installed on beamline 26 at the ESRF in Grenoble. A brief description of the beamline is given and then several components of the spectrograph are covered in more detail. Results of experiments performed both with direct non-monochromatized undulator radiation and with monochromatized radiation are reported.

**Keywords:** soft X-rays; X-ray emission spectrograph; fluorescence; X-ray scattering.

### 1. Introduction

In soft X-ray spectroscopy a rapidly developing field is core-emission spectroscopy (XES; X-ray emission spectroscopy) excited with synchrotron radiation. A very important contribution has been made in recent years by the Uppsala group (see Nordgren & Wassdahl, 1990) opening new perspectives in the study of the occupied valence states of solids. In XES, the spectrum of the valence-to-core transitions is measured as a function of the emitted photon energy. XES gives an 'image' of the occupied states complementing the more common core-absorption spectroscopy (XAS).

The perspectives in XES are particularly interesting in connection with third-generation synchrotrons. The main difficulty comes from the small fluorescence yield. The counting rate is the limiting factor because a significant experiment requires a resolving power greater than 1000.

In this field the ESRF (European Synchrotron Radiation Facility) can have a very specific and advanced role. The ESRF is not a soft X-ray source, being a 6 GeV machine; however, it is a very convenient machine to work down to soft X-rays with helical undulators. The first helical undulator (Helios I) installed at the ESRF has now been successfully operated down to *ca* 550 eV (Elleaume, 1990). Thus, a specific research area at the ESRF is XES on magnetic systems by exploiting polarization effects in the study of emission dichroism. This process was observed for the first time by Hague at LURE (Hague, Mariot, Strange, Durham & Gyroffly, 1993).

XES dichroism is the main goal of the AXES (Advanced X-ray Emission Spectrograph)\* project presented here. This instrument has been designed with the purpose of fully

exploiting the performance of beamline 26 (Goulon *et al.*, 1995) based on the helical undulator Helios I. Two distinct excitation procedures are considered:

(i) Direct excitation by non-monochromatized undulator radiation (hereafter referred to as quasi-monochromatic excitation). In this case, in contrast to dipole or wiggler radiation, the excitation is confined in an energy window (in our case *ca* 10% FWHM). The fundamental harmonic can be placed well above threshold (typically 200–300 eV above), so that mixing of threshold and above-threshold excitations is avoided. This removes the difficulties typical of white-beam excitation. The advantage is obviously in the counting rate.

(ii) Resonant excitation, the study of which is important in itself and requires monochromatic radiation.

On this basis we have decided that the AXES apparatus should be placed before the entrance slit of the beamline monochromator for most of the time so that it is possible, by lowering the sample to intersect the synchrotron radiation beam, to measure spectra at any moment. When the sample is raised the beam goes through AXES and there is no interference with other activities of the beamline. When AXES is used in experiments with monochromatic excitation it is moved past the beamline monochromator (Fig. 1).

The goal was to build an apparatus with a resolving power of at least 2000 with the flexibility of grating optics. It should be ready to use future innovative detectors (such as CCD detectors for soft X-rays) requiring normal incidence of the X-rays on the detector surface. The instrument was also required to collect the whole spectrum simultaneously in an energy window fixed at *ca* 40 eV. The main operation range of AXES corresponds to the  $L_{2,3}$  levels of the magnetic 3d transition metals (Fe around 700 eV) and the  $M$ -edges of the magnetic rare earths (Gd around 1200 eV). These goals make the instrument different from other XES

\* The AXES instrument is entirely supported by Italy through the INFN and INFN-CNR contracts.

spectrographs (Callcott, Tsang, Zhang, Ederer & Arakawa, 1986; Nordgren *et al.*, 1989) based on spherical gratings and using a Rowland mounting. A Rowland instrument necessarily has grazing incidence of the X-rays on the detector. An advantage of this geometry is that the spatial resolution of the detector is not a limiting factor due to the large dispersion along the detector surface. However, with traditional detectors the grazing incidence detection efficiency is much smaller than at normal incidence. Moreover, a Rowland system is incompatible with innovative detectors requiring normal incidence.

In the AXES case, the incidence of the photons is normal to the detector since we use a holographically corrected spherical grating (see §3). A scheme of the spectrograph

is given in Fig. 2. The sample is mounted on a vertical manipulator. The emitted X-rays pass through the input slit of the spectrograph, which has a horizontal input arm, and reach a grating that disperses in the vertical plane onto a movable detector. The spatial resolution of the detector is the limiting factor due to obvious geometrical reasons. This sets a lower limit to the length of the optical path and in fact AXES is longer than Rowland spectrographs used in XES excited with synchrotron radiation. This does not imply that the throughput is lower since this is basically defined by the dimension of the detector (for a given detector the horizontal aperture becomes larger in a shorter machine, but the slits must be narrower to obtain the same resolving power).

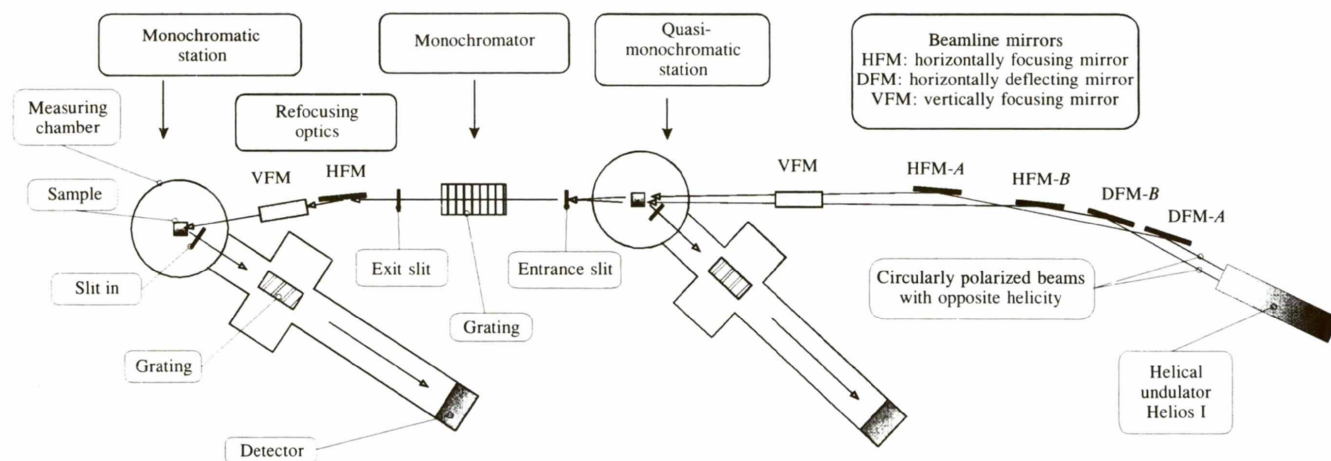


**Figure 1**

Functional layout of beamline 26 at the ESRF with the AXES instrument installed in the two possible positions.

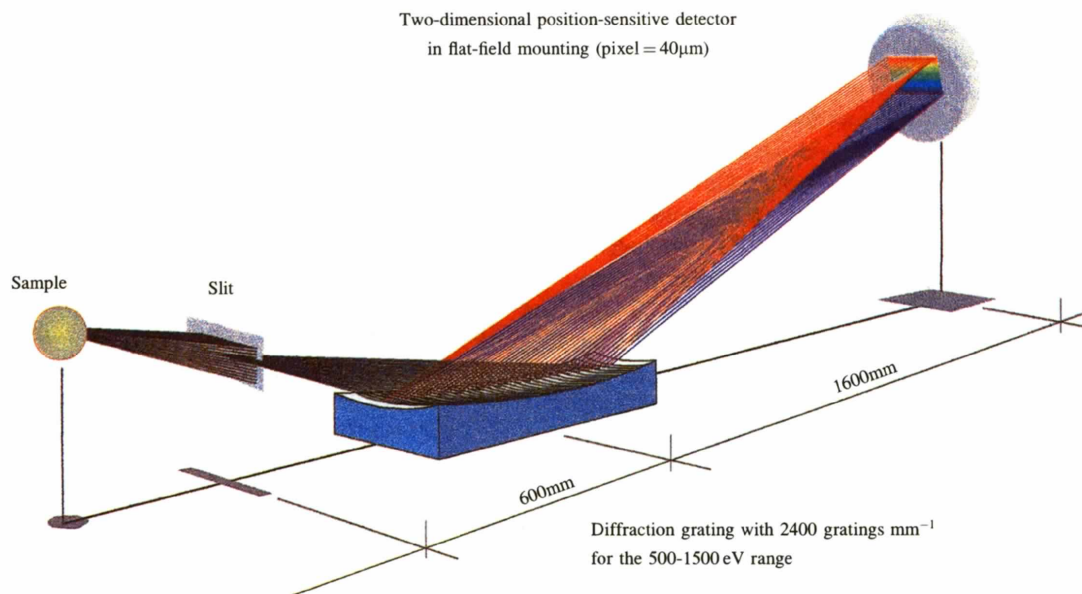


**Figure 2**

Conceptual scheme of the AXES instrument.

## 2. General description of the beamline

The AXES instrument is installed in the side-branch beamline (BL26) situated on the Helios I undulator.

Helios I is segmented into two identical modules separated by a magnetic chicane; this produces two synchrotron radiation beams (angle < 350  $\mu$ rad). The relative phases of the two modules of Helios I are chosen in order to minimize the perturbation on the electron orbit. Thus, one obtains two beams of opposite circular polarization in the beamline. Each module consists of nine periods of 85 mm, *i.e.* 765 mm long in total.

The soft part of the emitted radiation (below *ca* 2 keV) is deflected by a plane mirror in the side branch, which is equipped with Kirkpatrick–Baez refocusing optics using the same concept as described by Chen (1987). The use of a plane deflection mirror (DFM) before the horizontally focusing mirror (HFM) is necessary to reduce the thermal load on a delicate component. The vertically focusing mirror (VFM) is located after the horizontally focusing mirror. Typical thermal loads are 35 W on the plane deflection mirror and 2 W on the vertically focusing mirror at 800 eV and with a current of 100 mA in the ring. The mirrors are made from platinum-coated CVD silicon carbide and are water-cooled. The vertically focusing mirror gives a focus of *ca* 30  $\mu$ m FWHM at the entrance slit of the beamline monochromator, 7.55 m past the vertically focusing mirror. The vertically focusing mirror is the same for the two beams while separate independent horizontally focusing mirrors are used for the two beams. The beamline monochromator is of Dragon-like design (Chen, 1987) and has three interchangeable gratings.

When working in the quasi-monochromatic mode, AXES is placed *ca* 80 cm before the input slit of the Dragon monochromator so that the spot in a plane normal to the beam has a horizontal dimension of  $\sim$ 1.5 mm and a vertical dimension of  $\sim$ 350  $\mu$ m. The estimated flux at the sample is  $2 \times 10^{15}$  photons  $s^{-1}$  when the harmonic is centred at 1.7 keV with 100 mA current in the ring and having a 2.2  $\times$  2.2 pinhole defining the undulator beam at 26.64 m. Only a fraction of the flux ( $\sim$ 1/10) is used since the input slit of AXES is much smaller than the vertical height of the image on the sample. A future development could be to focus onto the sample; however, this option might create problems with delicate samples because of the increase in the power density.\* When working with monochromatic excitation, AXES is displaced past the Dragon monochromator; in this case the refocusing is crucial and is achieved with a dedicated Kirkpatrick–Baez optics that demagnifies about nine times in the vertical direction and six times in the horizontal.

AXES is equipped with a chamber allowing the installation of the instrument with the optical axes in different directions with respect to the synchrotron radiation (not without breaking the vacuum). The maximum angle is

75° allowing grazing incidence and near-normal emission, which is the best geometry to reduce self-absorption artifacts. This is crucial in emission dichroism since the emitted radiation is circularly polarized so that self-absorption can simulate an emission dichroism due to dichroism in absorption.

## 3. The grating

### 3.1. Design procedure

The grating was designed and built by the Jobin-Yvon company. The design takes full advantage of the aberration-control possibilities given by the holographic technique and is well understood using the Fermat principle.

In a non-holographic (*i.e.* ‘classical’) case, the path difference  $\Delta = (AM + MB) - (AV + VB) - kn\lambda$  has to be minimized, where *A* is the source, *B* the image, *M*(*X*,*Y*,*Z*) is a generic point on the grating, and *V* is the vertex, according to the coordinate system in Fig. 3.  $L_A$  and  $\alpha$  are the coordinates of *A*,  $L_B$  and  $\beta$  are the coordinates of *B*, *k* is the diffraction order,  $\lambda$  the wavelength, and *n* is the number of grooves between *V* and *M*. In the holographic approach, the Fermat principle has to be respected both in the use of the grating and in the generation of the hologram obtained with the recording points *C* and *D*, *i.e.* the two light sources which produce the groove pattern of the grating by interference (see Fig. 3). The two contributions can be combined by eliminating *n* so that the path difference  $\Delta$  contains the ‘classical’ and the corresponding ‘holographic’ terms. By introducing the coordinates of the holographic recording points *C*( $L_C, \gamma$ ) and *D*( $L_D, \delta$ ) and the radius of curvature *R* of the spherical grating, the function to be minimized is:

$$\begin{aligned} \Delta = & -Y[(\sin \alpha + \sin \beta) - H(\sin \gamma - \sin \delta)] \\ & + (Y^2/2)\{[D(L_A, \alpha, R) + D(L_B, \beta, R)] \\ & - H[D(L_C, \gamma, R) - D(L_D, \delta, R)]\} \\ & + (Z^2/2)\{[A(L_A, \alpha, R) + A(L_B, \beta, R)] \\ & - H[A(L_C, \gamma, R) - A(L_D, \delta, R)]\} \\ & + (Y^3/2)\{[C_1(L_A, \alpha, R) + C_1(L_B, \beta, R)] \\ & - H[C_1(L_C, \gamma, R) - C_1(L_D, \delta, R)]\} \\ & + (YZ^2/2)\{[C_2(L_A, \alpha, R) + C_2(L_B, \beta, R)] \\ & - H[C_2(L_C, \gamma, R) - C_2(L_D, \delta, R)]\} \\ & + \text{higher order terms.} \end{aligned} \quad (1)$$

The first line in the formula is the grating equation; other lines are the tangential defocus, the astigmatism, and the first and the second coma. The factor *H* multiplying the holographic terms is  $H = (k\lambda/\lambda_0)$ , where  $\lambda$  is the working wavelength and  $\lambda_0$  the recording wavelength. The functions *D*, *A*, *C*<sub>1</sub> and *C*<sub>2</sub> have the standard expressions defined in the calculation of the aberrant path of spherical gratings (Born & Wolf, 1959).

For each set of coordinates ( $L_A, \alpha, L_B, \beta$ ) the recording parameters ( $L_C, \gamma, L_D, \delta$ ) are available to cancel the

\* We have already encountered problems with Ce compounds such as CeCo<sub>2</sub>.

classical terms in assigned points of the space. In our case we selected the input angle  $\alpha = 88^\circ$  in order to have a reasonable reflectivity. The optimization was made by forcing the diffracted spectrum onto a flat field perpendicular to the diffracted rays. This introduces an off-Rowland defocusing that comes from the classical tangential term. This is compensated for by optimizing the holographic tangential defocus and sagittal defocus. Besides these conditions, coma 1 and coma 2 were minimized. The work was performed iteratively to find a solution compatible with the constraints (slit size and desired dimensions of the instrument). Within these constraints one obtains the grating parameters minimizing all aberrations up to third-order terms, and the values of  $L_B$  and  $\beta$  versus wavelength. The result of the optimization is a grating having a radius of curvature  $R = 30\,150$  mm, input arm  $L_A = 597.8$  mm, output arm  $L_B \simeq 1600$  mm,  $N = 2400$  gratings  $\text{mm}^{-1}$  and an  $88^\circ$  angle of incidence, with a  $20\ \mu\text{m}$  input slit and a  $20\ \mu\text{m}$  resolution on the detector. The horizontal aperture (*i.e.* in the plane perpendicular to the dispersion plane) can reach 12 mrad if the detector has a useful diameter of up to 40 mm.

### 3.2. Results on the grating

The grating used so far has been optimized to study  $L_{2,3}$  emission from 3d magnetic transition metals (700–900 eV).

The focal position is very different with respect to the corresponding Rowland mounting. The focal position is given in Fig. 4 where  $h$  and  $v$  are the horizontal and vertical distances of the centre of the flat field with respect to the centre of the grating, the input arm being horizontal.

The design was tested by ray tracing; we show a few significant examples in Fig. 5. The slits were set to 10 and  $20\ \mu\text{m}$ , respectively, and the horizontal dimension of the source was 1.5 mm. The resolving power (defined as  $\lambda/\Delta\lambda$ , where  $\Delta\lambda = \text{FWHM}$ ) of the holographic grating is compared with the resolving power of a Rowland grating having the same parameters and used with a hypothetical flat detector perpendicular to the diffracted rays with its

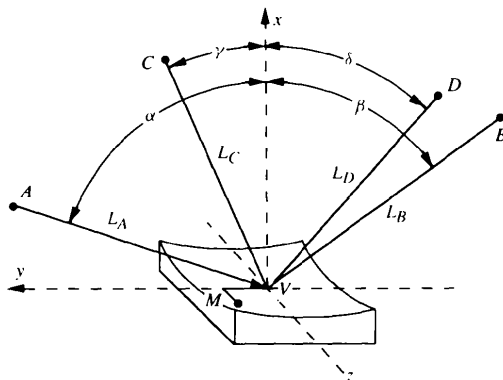


**Figure 3**

Coordinate system for a holographically recorded diffraction grating:  $A$  is the source,  $B$  the image,  $C$  and  $D$  the recording points,  $M$  a generic point of the grating,  $V$  the vertex.

centre on the Rowland circle. Figs. 5(a), 5(b) and 5(c) refer to a vertical input aperture (*i.e.* in the dispersion plane) of 2 mrad. The detection out of the Rowland circle drastically degrades the resolution in a Rowland mounting, while in the holographically corrected spherical grating the resolving power is basically constant in an energy window of ca 40 eV.

The effect of the vertical aperture (*i.e.* in the dispersion plane) has also been studied by calculating the 2, 3 and 4 mrad cases. The vertical aperture can be changed with movable masks that can be inserted in front of the grating. The effect of the vertical aperture on the line shape is shown in Fig. 6, where we present ray-tracing data at three energies in the working range of the instrument. The data in the left and right panels pertain to two detectors having 20 and  $45\ \mu\text{m}$  resolution, respectively. The increase of the vertical aperture increases the linewidth and introduces an undesirable asymmetry. With  $20\ \mu\text{m}$  resolution of the detector (left panel) no asymmetry is seen with a 2 mrad aperture at all energies, at a 3 mrad vertical aperture a tiny asymmetry is seen at low energy, and at a 4 mrad vertical aperture a tiny asymmetry is seen at medium and high energies, while the line shape is not acceptable at low energy, where a marked shoulder is seen. The system is more sensitive to the vertical aperture when the dispersion increases. In the case of a detector with a lower spatial resolution (right panel) the system is less sensitive to the asymmetry, and the performance at 4 mrad is totally

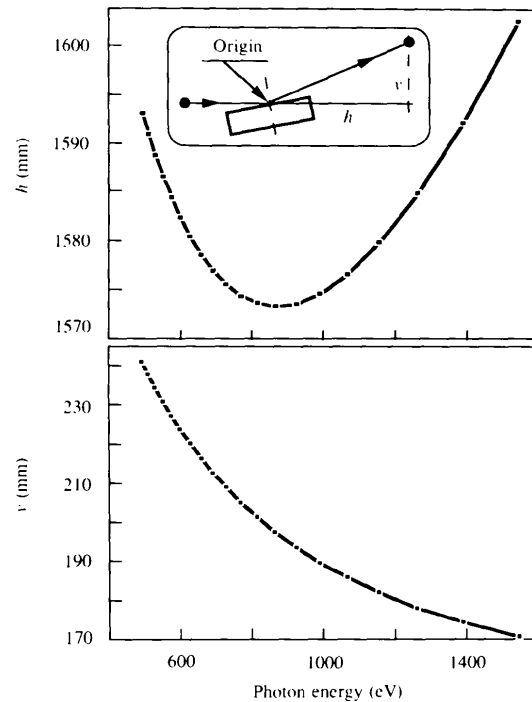


**Figure 4**

Focal position of the spectrum given by the grating:  $h$  and  $v$  are the horizontal and vertical distances of the centre of the flat field with respect to the centre of the grating, the input arm being horizontal. Note that the horizontal coordinate is not monotonic as a function of photon energy.

acceptable above 700 eV, the shape being controlled by the dispersion. At lower energy, a small asymmetry is still seen.

The spectrometer is used at present in conditions close to those of the right-hand panel, with the whole grating illuminated (corresponding to 3 mrad). Marginal improvement is obtained by masking, unless one works at low energies where masking is compulsory.

#### 4. Other information on the components

The instrument is installed on a very rigid mechanical support allowing displacements without affecting the internal optical alignment. The mechanical support allows the spectrograph to be moved accurately to fit to the beamline. The detector is displaced to the appropriate position by moving a motorized output arm with an (X,Y) mechanism connected to a computer. The positions are read with linear encoders with a resolution of 1  $\mu\text{m}$ .

In the present set-up the detector is a micro-channel plate with resistive anode encoder consisting of a stack of three plates in the Venetian window or 'Z' geometry.\* The diameter of the detector is *ca* 20 mm and the resolution

\* Supplied by Photek Ltd.

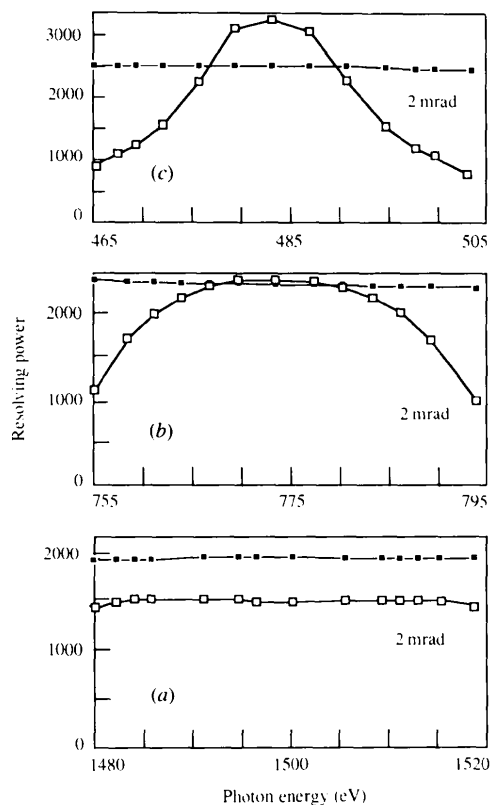


**Figure 5**

Resolving power (10 and 20  $\mu\text{m}$  slits with 1.5 mm horizontal acceptance) for the holographic grating (filled squares) and for the corresponding Rowland grating (open squares) having the same parameters and used with a hypothetical flat detector perpendicular to the diffracted rays with its centre on the Rowland circle. The resolving power is defined as  $\lambda/\Delta\lambda$ , where  $\Delta\lambda$  is the full width at half maximum. Data were obtained by ray-tracing by Jobin-Yvon.

is about *ca* 40  $\mu\text{m}$ , thus limiting the resolution, which is a factor of 0.7 lower than in Fig. 5. No special coatings or repeller grids are used since at near-normal incidence the efficiency can already reach 40% (Fraser & Pearson, 1984). In this case the incidence angle of the photons must be optimized to photoemit electrons from the edge of the channels. We have made the following provisions: (i) the zigzag channels of the micro-channel plate (MCP) stack are azimuthally oriented so that they are contained in the vertical plane; (ii) the detector can be pivoted around a horizontal axis contained in the detector surface.

Fig. 7 shows how the adjustment of the channels with respect to the photons affects the counting rate. The sharp minimum in the middle of the curve is due to the very good collimation of the X-rays; when the micro-channel plate channels are aligned with the propagation direction of the photons, photoemission takes place basically on the second plate with a great loss in gain.

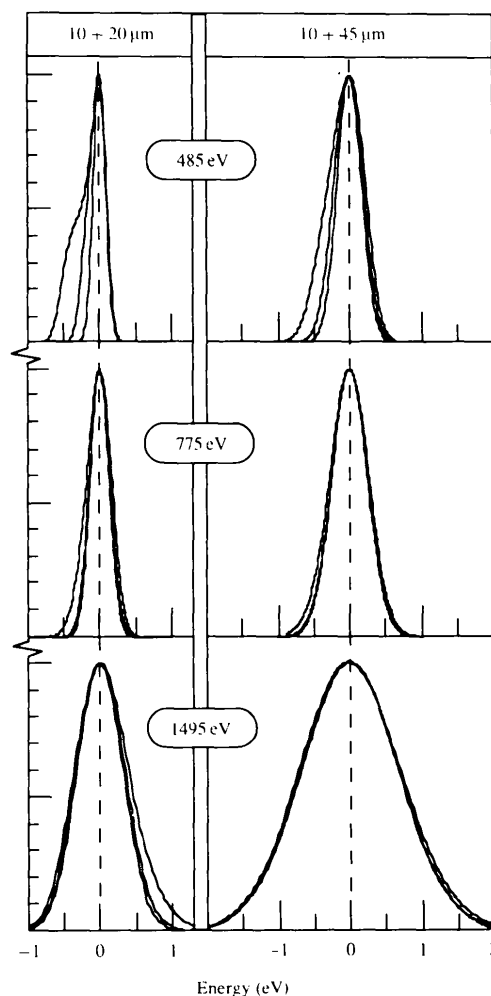


**Figure 6**

The effect on the line shape of the angular aperture along the dispersion direction for two detectors having 20 and 45  $\mu\text{m}$  resolution with a 10  $\mu\text{m}$  entrance slit. Line shapes are presented in the 2, 3 and 4 mrad cases; the curves are in some cases superimposed, otherwise they are easily identified as the line width increases with aperture.

The detector is controlled by a transputer installed on an MS-DOS personal computer with 486 microprocessor. The image of the detector is transferred from the transputer to the computer in order to calculate and then save the spectra. The acquisition computer can also control the beamline vertically focusing mirror so that the optimal vertical position of the spot seen by the input slit of AXES can be found by maximizing the counting rate.

In the dichroism measurements, we use a special magnetic circuit to magnetize the sample along the surface in the horizontal direction (Dallera, Ghiringhelli & Braicovich, 1996). In magnetic measurements, AXES can be operated in four modes:

(i) One mode uses only one beam from Helios I with a given polarization and the magnetization of the sample is periodically reversed to minimize all effects coming from long-term drifts.

(ii) When it is not possible to reverse the magnetization easily one changes from one beam to the other having opposite polarization; this is achieved with a dedicated chopper installed on the beamline past the vertically focusing mirror in a position where the two beams are separated by *ca* 4 mm; the two beams are deflected onto the same position on the sample by using the horizontally focusing mirrors. Because of the difference in intensity of the two beams the normalization to  $I_0$  is particularly important.

(iii) A combination of the two methods with sequential change of the polarization and of the magnetization is useful to extract the intrinsic asymmetry of the whole system.

(iv) The fourth mode involves reversing the phase of the undulator.

## 5. Performance of the system

The machine has been tested both with quasi-monochromatic and with monochromatic excitation. Some of the results are described below.

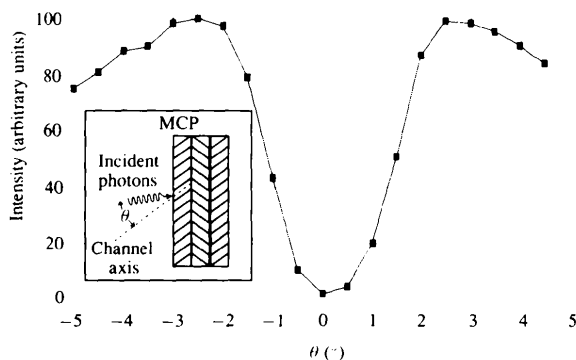


**Figure 7**

Counting rate in arbitrary units as a function of the angle between the incident photons and first micro-channel plate axis. The counting rate has a very sharp minimum in the middle when the micro-channel plate channels are aligned with the X-rays.

## 5.1. Quasi-monochromatic excitation

We show that with direct excitation by undulator radiation the sensitivity is increased so that it is possible to measure, with an excellent signal-to-noise ratio, the spectral functions of minority components down to the  $10^{-3}$  concentration range.

A study was performed of the electronic states of the inhomogeneous Al-rich Al-Cu alloy during aging. We concentrated on the  $\theta'$  phase and on the final equilibrium  $\theta$  phase. Both phases have the  $\text{CuAl}_2$  composition, but only the  $\theta$  phase has the C16 structure typical of bulk  $\text{CuAl}_2$ . The  $\theta'$ -phase sample was prepared by thermal aging of the Al-Cu 0.5 at.% alloy. The measurements were taken with excitation by the first harmonic of the undulator peak at 1700 eV (FWHM = 250 eV). The flux at the sample was *ca*  $10^{15}$  photons  $\text{s}^{-1}$  (100 mA) $^{-1}$  and this allowed the whole spectral function of 0.5% Cu in Al to be measured in 3 h.

The Cu  $L_3$  XES spectra from the  $\theta'$  phase and from a C16- $\text{CuAl}_2$  single crystal measured in strictly comparable conditions are shown in Fig. 8. In the  $\theta'$  phase a narrowing of the Cu 3d band is seen which is most likely related to different atomic environments. In fact, in the  $\theta'$  phase the four first and eight second Cu neighbours of Cu atoms are at 4.04 and 4.07 Å, while in the  $\theta$  phase the two first neighbours are at 2.44 Å and the four second neighbours are much further away. Therefore, in the  $\theta'$  phase the d band due to the (Cu 3d-Cu 3d) interaction is narrower because of the rapid decrease of the interatomic integrals with decreasing overlap. The present results are the first spectroscopic evidence of this effect (Dallera, De Michelis, Puppini, Braicovich & Brookes, 1996).

## 5.2. Monochromatic excitation

We present, as a result exploiting the polarization of the X-rays, a study of a magnetic alloy by the technique of emission magnetic circular dichroism (EMCD). EMCD

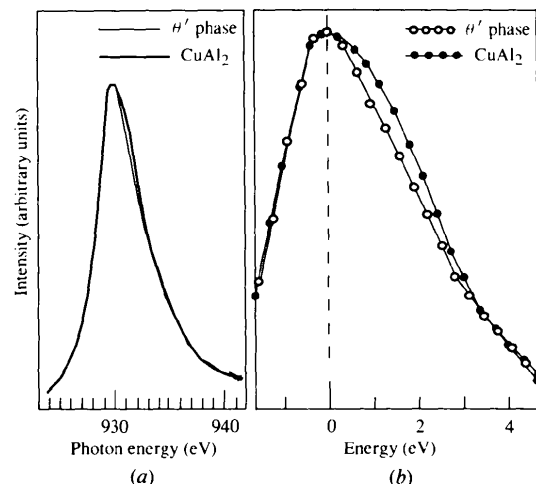


**Figure 8**

(a) An overview of the  $L_3$  emission spectra in Cu-Al  $\theta'$  phase and in crystalline  $\text{CuAl}_2$  ( $\theta$  phase). (b) An enlarged view of the peak region.

is the difference between the intensity of the emitted spectra excited with circularly polarized light of opposite helicity. It has been demonstrated by Strange, Durham & Gyorfy (1991) that this difference closely reflects the spin-resolved local occupied density of states. The possibility of measuring EMCD has been demonstrated by Hague *et al.* (1993) at LURE on a bending-magnet beamline in the case of the  $L_{2,3}$  emission of Fe. After a test on Fe dichroism with quasi-monochromatic undulator excitation, we performed experiments on magnetic alloys with monochromatic excitation. The 'as measured' EMCD spectra of Fe  $L_3$  in the alloy  $\text{Fe}_{0.05}\text{Co}_{0.95}$  are shown in Fig. 9. The sample was a 600 Å-thick film evaporated on an Si(100) substrate and capped with a 20 Å-thick Cr layer. It was magnetized with a magnetic circuit described by Dallera, Ghiringhelli & Braicovich (1996). The magnetic field was parallel to the sample and the X-rays were incident on the sample at a 20° angle from the surface. The emission was normal in order to avoid dichroism in self-absorption along the exit path. The spectra were taken reversing the magnetic field direction every 5 min. The monochromator energy was set at 706.5 eV and the entrance and exit slits were opened up to 200 and 600 μm, respectively. In this situation the band pass was *ca* 3 eV FWHM. The counting rate was 15 counts s<sup>-1</sup> over the whole detector, but the background was very low (the signal-to-noise ratio was always > 15) and the spectrum was measured in 8 h. This is the first time EMCD has been measured on a minority component.

The experimental results shown in Fig. 9 demonstrate that very large effects can be measured in contrast to other

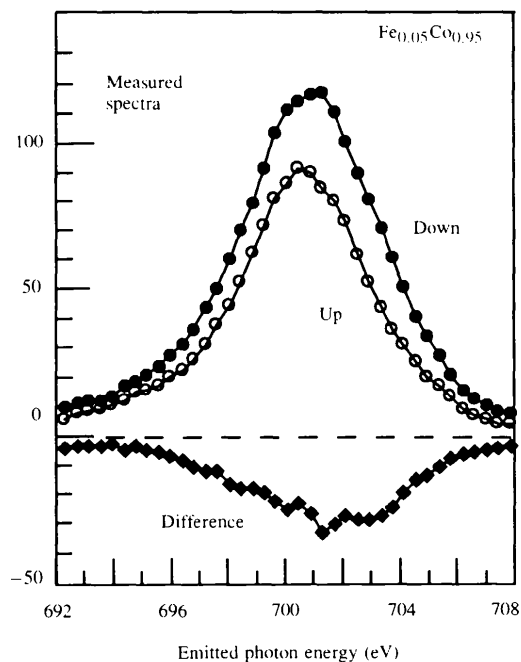


**Figure 9**  
'As measured' EMCD spectra of Fe  $L_3$  in the alloy  $\text{Fe}_{0.05}\text{Co}_{0.95}$ . The mean value of the two spectra at their maximum has been set to 100.

published cases (Duda *et al.*, 1994; Hague, Mariot, Guo, Hricovini & Krill, 1995); the results deserve the following comments:

(a) The measured dichroism comes from a combination of dichroism in the excitation and in the decay channels. In fact, the incoming radiation excites a core electron into the valence band, and the core hole which is left behind is neutralized by the radiative decay of a valence electron. In this schematic view the absorption magnetic circular dichroism is controlled by the spin of the empty states and the decay channel by the spin of the occupied states. In a system such as Fe, having empty states dominated by minority spin and occupied states dominated by majority spin, this gives rise to a reduction of the value of EMCD with respect to absorption magnetic circular dichroism as is found in the present example.

(b) The line shapes of the spectral functions with opposite helicities are different. This shows that the two curves are not exclusively controlled by absorption dichroism: if this was the case, there would be a re-scaling factor able to superimpose the two curves, as absorption dichroism is constant since the incoming energy is fixed. Thus, the spectra also give information on dichroism in the de-excitation channel. This information is connected with the polarization of occupied  $d$  states.

(c) Since in a disordered alloy  $k$  does not have a well defined value, there is no restriction on the emitted photon momenta imposed by momentum conservation, and absorbed and emitted photons do not interfere. Therefore, a simplified model based on the incoherent product of absorption and emission can be used as a first approximation (Ma & Blume, 1995). The dichroism in the emission channel is opposite to that in the absorption channel, and the emission channel is dominated by the contribution from the filled majority-spin electrons. We anticipate that a systematic work on Fe-Co alloys, still in progress, will show for the first time that the emission dichroism correlates with the magnetic properties; in particular, the filling of majority spin states of Fe upon alloying with Co (Schwarz, Mohn, Blaha & Kübler, 1984) is seen.

The authors would like to thank the Jobin Yvon staff for cooperation in preparing §3. The constant and invaluable involvement of J. Goulon in the project is greatly acknowledged. One of us (LB) is particularly indebted to F. Sette for crucial support and constructive discussions in the early stage of the project.

## References

- Born, M. & Wolf, E. (1959). *Principles of Optics*, pp. 202–231. London: Pergamon Press.
- Callcott, T. A., Tsang, K. L., Zhang, C. H., Ederer, D. L. & Arakawa, E. T. (1986). *Rev. Sci. Instrum.* **57**, 2680–2690.
- Chen, C. T. (1987). *Nucl. Instrum. Methods*, **A256**, 595–604.
- Dallera, C., De Michelis, B., Puppini, E., Braicovich, L. & Brookes, N. B. (1996). *Phys. Rev. B*, **53**, 965–968.
- Dallera, C., Ghiringhelli, G. & Braicovich, L. (1996). *Rev. Sci. Instrum.* **67**, 355–357.

- Duda, L.-C., Stöhr, J., Mancini, D. C., Nilsson, A., Wassdahl, N., Nordgren, J. & Samant, M. G. (1994). *Phys. Rev. B*, **50**, 16758–16761.
- Elleaume, P. (1990). *Nucl. Instrum. Methods*, **A291**, 371–377.
- Fraser, G. W. & Pearson, J. F. (1984). *Nucl. Instrum. Methods*, **219**, 199–212.
- Goulon, J., Brookes, N. B., Gauthier, C., Goedkoop, J., Goulon-Ginet, C., Hagelstein, M. & Rogalev, A. (1995). *Physica B*, **208/209**, 199–202.
- Hague, C. F., Mariot, J.-M., Guo, G. Y., Hricovini, K. & Krill, G. (1995). *Phys. Rev. B*, **51**, 1370–1373.
- Hague, C. F., Mariot, J.-M., Strange, P., Durham, P. J. & Gyorffy, B. L. (1993). *Phys. Rev. B*, **48**, 3560–3562.
- Ma, Y. & Blume, M. (1995). *Rev. Sci. Instrum.* **66**, 1543–1545.
- Nordgren, J., Bray, G., Cramm, S., Nyholm, R., Rubensson, J.-E. & Wassdahl, N. (1989). *Rev. Sci. Instrum.* **60**, 1690–1696.
- Nordgren, J. & Wassdahl, N. (1990). *Phys. Scr.* **T31**, 103–111.
- Schwarz, K., Mohn, P., Blaha, P. & Kübler, J. (1984). *J. Phys. F*, **14**, 2659–2671.
- Strange, P., Durham, P. J. & Gyorffy, B. L. (1991). *Phys. Rev. Lett.* **67**, 3590–3593.